Colloids and Surfaces A: Physicochemical and Engineering Aspects 689 (2024) 133722

Contents lists available at ScienceDirect

Colloids and Surfaces A: Physicochemical and Engineering Aspects

journal homepage: www.elsevier.com/locate/colsurfa

Preparation of mechanically durable superhydrophobic aluminum surfaces by LST/MAO and chemical modification

Qiqi Wu, Jing Xu, Nan Tu, Bowen Xue, Jian Chen, Hailin Lu *

Group of Mechanical and Biomedical Engineering, College of Mechanical & Electronic Engineering, Xi'an Polytechnic University, Xi'an, Shaanxi 710048, PR China

GRAPHICAL ABSTRACT

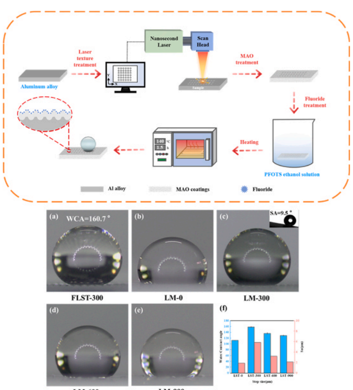

ARTICLE INFO

Keywords:
Micro-arc oxidation
Laser surface texturing
Superhydrophobic surfaces
Mechanical durability
Corrosion resistance

ABSTRACT

In this paper, a superhydrophobic surface with mechanical durability was prepared on 6061 aluminum (Al) alloy by combining laser surface texturing (LST) and micro-arc oxidation (MAO) techniques followed by chemical immersion treatment. The effects of processing on Al alloys with different texturing spacings on the surface morphology, roughness, surface wettability, and corrosion resistance of the subsequently formed composite coatings were analyzed. The results show that a superhydrophobic surface was obtained with the water contract angle (WCA) of 158.3 ° and the roll-off angle of 9.5 ° at a texture spacing of 300 μm. This was due to the fact that the surface microroughness texturization process created by LST on the surface increased the generation of surface nanostructures, and combined with the natural nanostructure possessed by MAO, unique " double " nanostructure was formed on the surface. This surface structure increased the area of fluoride attachment, reduced the solid-liquid contact area, and decreased the adhesion of droplets to the surface, resulting in higher hydrophobicity. Electrochemical corrosion experiment showed that the corrosion current density of LM-300 was 2 orders of magnitude lower than that of the LM-0 sample, clearly demonstrating better corrosion resistance. In addition, the prepared superhydrophobic surface presented excellent mechanical durability, and in the ceramic zirconia cyclic abrasion experiment, the superhydrophobic surface was able to withstand 61 cycles of abrasion at a pressure of about 2.5 kPa.

* Corresponding author.
E-mail address: luhailinpro@163.com (H. Lu).

https://doi.org/10.1016/j.colsurfa.2024.133722
Received 20 November 2023; Received in revised form 6 March 2024; Accepted 14 March 2024
Available online 15 March 2024

1. Introduction

In recent years, functional surfaces with extreme wetting conditions have attracted significant attention in industrial, transportation, and medical applications due to their advantages such as self-cleaning, corrosion resistance, anti-freezing, and antibacterial properties [1–3]. Currently, the construction of superhydrophobic surfaces is mainly achieved through the combination of micro-nano hierarchical structures and low surface energy material modifications [4–7]. When the coating surface exhibits superhydrophobicity, it shows a strong repellent effect towards liquid corrosive media. This property effectively reduces the contact area between the corrosive media and the surface, thereby minimizing or preventing the penetration of the corrosive media. Therefore, it can further enhance the corrosion resistance of the substrate, prolonging the service life of anti-corrosion coatings and materials [8–10].

Surface texturing is the process of creating specific patterns on a surface to enhance its performance in its working environment. Typically, for most materials with small surface free energy, the wettability can be achieved by adjusting the microtexture of the surface to change the hydrophobicity of the surface [11]. In recent studies, LST has been developed as a promising method for fabricating superhydrophobic surfaces due to its process flexibility, ease of automation, and environmental friendliness [12]. Li [13] et al. prepared superhydrophilic/superhydrophobic surfaces on commercial titanium plates by a facile and efficient laser scanning process as well as simple silanization modifications, and investigated the effect of laser energy density on the structure and surface wettability. Lian [14] et al. proposed a method to prepare a bionic surface of taro leaves using direct laser interference lithography and hydrothermal treatment, and the prepared surface has good superhydrophobicity and anti-icing properties. Gao [15] et al. prepared bimodal surface structures with switchable and anisotropic/isotropic wettability on copper surfaces by laser processing, chemical etching, and mixed thiol modification, enabling the manipulation of both water/oil droplets and water/oil fluids. Therefore, it is a simple and practical method to construct nanostructures using LST to realize the preparation of superhydrophobic surfaces. So far, however, most of them have been the direct LST treatment on metal surfaces to study the effect on their hydrophobicity, yet there are few studies on the use of LST to regulate the rough surfaces formed by MAO to fabricate superhydrophobic surfaces. Our findings indicate that most LST construct hydrophobic surfaces are processed directly on the substrate and become hydrophobic/superhydrophobic after subsequent treatment by long-term exposure to organic contaminants in air [16], chemical modification with fluoroalkylsilanes [17], silica sols [18], or low-temperature annealing in a contaminated furnace [19]. Also, in most of the studies, the surface substrates of the prepared superhydrophobic samples are directly exposed to air or their surface is covered with relatively fragile coatings. Since the double-scale roughness may be irreversibly degraded, the nanostructure formed on the surface in some harsh environments may be susceptible to damage, leading to a decrease in hydrophobicity [20]. In summary, it is necessary to protect the hierarchical surface structure formed after LST treatment, to extend their service life in harsh environments.

MAO is a technique developed based on anodization. This method involves using metals or their alloys such as titanium (Ti), magnesium (Mg) and Al as the anode and placing them in a container filled with an electrolyte. The electrochemical reactions that occur during this process lead to the formation of a dense ceramic oxide film on the surface [21,22]. When the high-temperature pulsed laser weaves the surface of the substrate, then a ceramic coating is formed on the surface using the MAO process. The ceramic film layer not only has high bonding strength and can be tightly bonded to the substrate, but also has high hardness and structural stability [23,24]. Therefore, it is beneficial to improve the mechanical abrasion and corrosion resistance of superhydrophobic sample. Thus, it will improve the mechanical abrasion resistance and corrosion resistance of the superhydrophobic samples. At the same time, ceramic films generally exhibit a "crater-like" rough porous nanostructure, and the micropores and microcracks in the outer layer provide mechanical interlocking sites that enhance the adhesion of organic or polymer topcoats to the substrate [25]. Moreover, the study of combining LST and MAO techniques to prepare superhydrophobic surfaces is still relatively scant, which has certain research value.

Herein, we prepared a mechanically durable superhydrophobic surface by chemically modifying a 6061 Al disk after LST/MAO treatment followed by immersion in a fluorosilane solution. The influence of different LST spacings on the surface morphology, roughness, surface wettability and corrosion resistance of composite coating was investigated, and the mechanism of wettability change was discussed. The physical properties of the coatings were characterized by scanning electron microscopy (SEM), X-ray photoelectron spectroscopy (XPS), and X-ray diffraction (XRD). Also, corrosion resistance and mechanical stability were evaluated by potentiodynamic polarization (PDP) curves, electrochemical impedance spectroscopy (EIS), friction experiment and abrasion experiment.

2. Experimental

2.1. Materials

Al disks with a diameter of 30 mm and a thickness of 5 mm were used. Sodium hexametaphosphate ($(NaPO_3)_6$), sodium hydroxide (NaOH), polyethylene glycol (PEG), and sodium silicate ($NaSiO_3 \cdot 9H_2O$) produced by Tianjin Damao Chemical Reagent Factory. Anhydrous ethanol (CH_3CH_2OH) from Tianjin Fuyu Fine Chemical Co. 1 H, 1 H, 2 H, 2 H-perfluorooctyltrichlorosilane (PFOCTS, $C_8H_4F_{13}$-Si≡Cl) produced by Shanghai McLean Biochemistry and Technology Co. All reagents used herein are analytical grade reagents (AR).

2.2. Preparation of superhydrophobic surfaces

Al disk with silicon carbide sandpaper #600, #2000 and polishing cloth in sequence. The polished samples were then cleaned by ultrasonic cleaning with anhydrous ethanol, and deionized water, respectively, for 10 minutes to remove surface residues. A fiber laser marking machine (JL-F50, wavelength 1064 nm, spot size 100 μm) was used. The laser processing parameters were: laser frequency of 20 kHz, power of 50 W, scanning speed of 1000 mm/s. The laser beam was dotted along the x-axis and then along the y-axis on the surface of the treated Al disk with five scans, forming circular pits with a diameter of 100 μm. The scanned area is 20 mm × 20 mm, forming a dot-matrix texturing with a surface texturing of 20 mm × 20 mm. The spacing between two adjacent circular pits was then varied to 300 μm, 600 μm, and 900 μm to obtain weaving patterns with different spacing on the surface of the Al disk. The laser-treated samples and untreated Al disks were subjected to MAO treatment using a bipolar microarc oxidizer. The electrolyte was formulated as: $(NaPO_3)_6$ 36 g/L, $NaSiO_3 \cdot 9H_2O$ 4 g/L, PEG 2 g/L, NaOH 1 g/L. The sample was then connected to the anode of the pulsed power supply and the stainless steel sheet to the negative electrode, after which they were placed in the formulated electrolyte for MAO treatment. A condenser was used to circulate the electrolyte into the electrolyte to cool the electrolyte to prevent overheating. After removal, the sample was placed into a beaker containing deionized water to ultrasonically clean the electrolytes remaining on the surface of the sample, then the cleaned sample was set aside at room temperature.

After that, 0.66 wt% 1 H,1 H,2 H,2 H-perfluorooctyltrichlorosilane ethanol solution was prepared by combining 1 H,1 H,2 H,2 H-perfluorooctyltrichlorosilane and anhydrous ethanol solution according to certain ratios. Finally, the spare samples were immersed in the prepared solution for 12 h. In the end, the samples were heated in a vacuum drying oven at 140 ℃ for 1 h. The experiment yielded four different samples, labeled as LM-0, LM-300, LM-600, and LM-900, respectively.

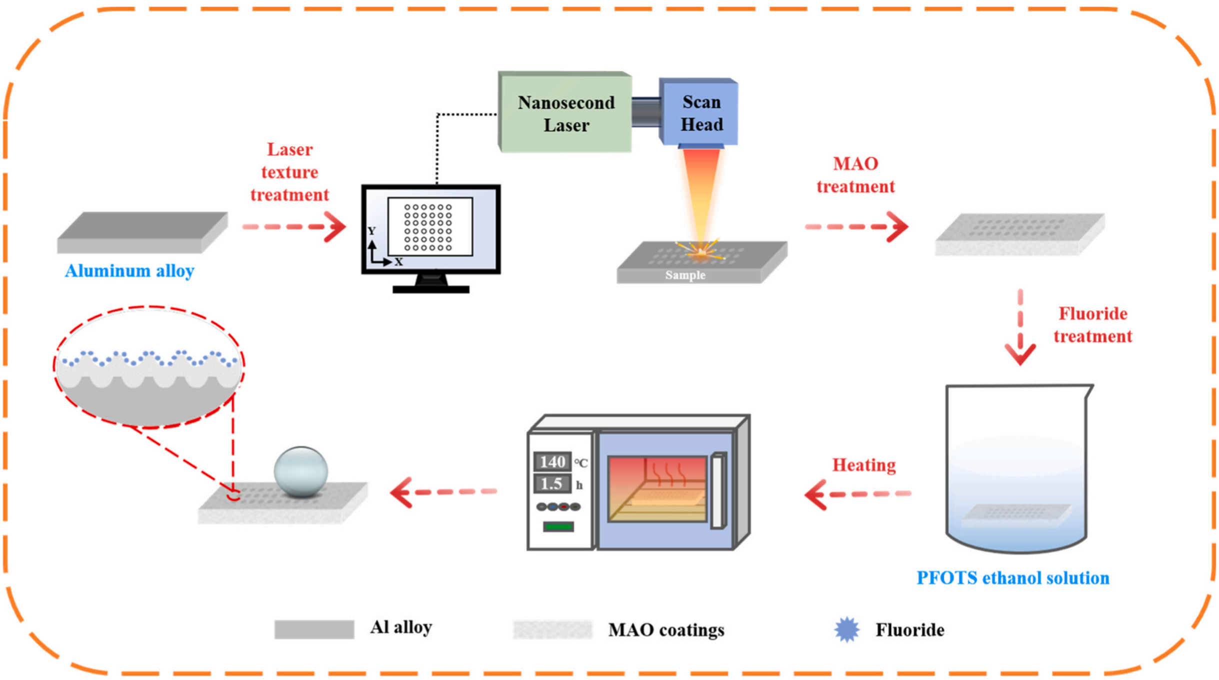

Fig. 1. Flow scheme of specimen preparation.

The LST only treated sample with a spacing of 300 μm was expressed as LST-300. In addition, the sample with a spacing of 300 μm that was treated with LST and hydrophobicity was expressed as FLST-300. The preparation process is illustrated in Fig. 1.

2.3. Friction experiment

Experiments using GSR-2 friction tester (China Rubber Alcohol Rubbing Tester, Shenzhen Zhijia Instrument & Equipment Co.) The friction properties of four samples (LM-0, LM-300, LM-600 and LM-900) were investigated under dry friction condition and water lubrication condition. A polyethylene ball of 9.5 mm diameter was chosen to be slidingly rubbed on the sample at room temperature (25–26 °C). The experimental load was 2 N, and the speed was 1 cm/s. In the water lubrication experiment, the contact surfaces of the friction pair were completely submerged in a deionized water solution. Each experiment was repeated three times under the same experimental conditions, and each friction test lasted 15 min. During the experiment, a force transducer was used to detect and collect data, followed by converting the data into electrical signals to be fed into a computer so that the coefficient of friction (COF) could be automatically recorded into the computer.

2.4. Abrasion experiment

The experiment uses GSR-2 friction tester (China Rubber Alcohol Rubbing Tester, Shenzhen Zhijia Instrument and Equipment Co.) The test investigated the mechanical abrasion resistance of LM-300. At room temperature (25–26 °C), a zirconia ceramic rod with a diameter of 10 mm was selected to be slidingly rubbed on the sample. The pressure of 2 N was applied to the zirconia ceramic rod at the speed of 1 cm/s. Each 10 mm back and forth rubbing was considered as one cycle. The 100 cyclic abrasion experiments were carried out, and the water contact angle (WCA) of the samples was measured after every 10 cyclic abrasion experiments and averaged over three measurements.

2.5. Electrochemical corrosion experiment

The CS350M electrochemical workstation was used to test the corrosion resistance of LM-0 and LM-300 in a conventional three-electrode cell. And the electrochemical impedance spectra of LM-0 and LM-300 as well as polarization curves were plotted to further analyze the changes in corrosion resistance. The experiment utilized the sample (working electrode), platinum foil (auxiliary electrode), and saturated KCl (reference electrode) as the conventional three-electrode cell setup. To reduce external interference, the setup was placed inside a Faraday cage. To obtain a stable open circuit potential (OCP), the samples with an area of 1.0 cm^2 were immersed in a 3.5% wt% NaCl solution for 60 min. In the experiment, the experimental parameter was set as follows: the initial potential was −0.1 V, the final potential was 0.1 V, the scan rate was 0.167 mV/s, and the duration of the experiment was 1.5 h.

2.6. Characterization

LST-300, LM-0 and LM-300 samples were characterized in the study. The phase composition of the samples was characterized using the X-ray diffraction (XRD) function of the D8 Advanced Diffractometer (Bruker, Germany). The grazing angle was set at 3 °, and Cu Kα radiation (40 kV, 40 mA) was used in the range of 10 ° to 90 ° with a scanning speed of 10 °/min. The elemental composition of the specimens was examined using energy dispersive spectroscopy (XPS) (Thermo Fisher Scientific, USA). The surface morphology of the specimens was analyzed by observation of JSM-6460LV scanning electron microscope (SEM) images. Photographs were taken of the textured morphology of the samples using a forward-facing metallurgical microscope (Shenzhen Oswald Optical Instrument Co., Ltd.). A Zegage 3D surface profiler was used to photograph the three-dimensional shape of the sample and measure the arithmetic mean surface roughness (Sa). The WCA was measured using an AO-V128 microscope (Shenzhen Oswald Optical Instrument Co., Ltd.). The roll-off angle of the samples was measured using Lauda Scientific LSA100, Germany. three measurements were taken and averaged as the measurement result.

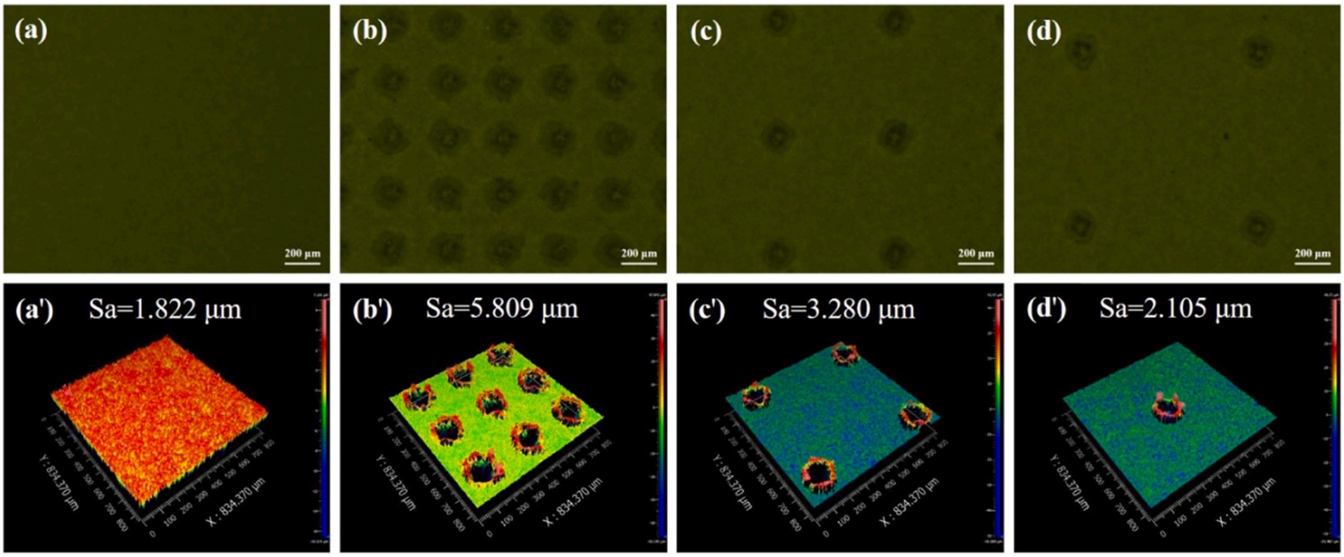

Fig. 2. Surface microscope images of the samples with different scanning spacings: (a) LM-0;(b) LM-300; (c) LM-600; (c) LM-900; 3D morphology of the samples with different scanning spacings: (a′) LM-0; (b′) LM-300; (c′) LM-600; (d′) LM-900.

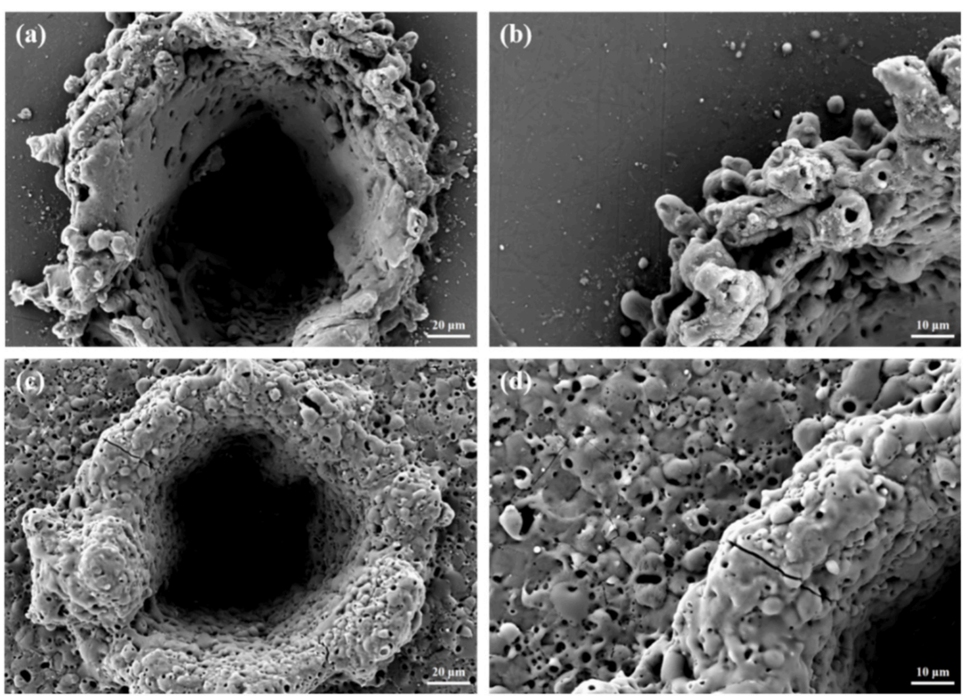

Fig. 3. . (a), (b) SEM images of LST-300 at 500 x and 1000 x magnification; (c), (d) SEM images of LM-300 at 500 x and 1000 x magnification.

3. Results and discussion

3.1. The analysis of microtopography

The surface morphology of the sample at different scanning spacings is shown in Fig. 2. As shown in Fig. 2a-d, it can be observed that the Al disk is covered with a rough ceramic coating after MAO treatment and a uniformly distributed dot texturing after LST treatment. It can be observed that as the scanning spacing increases, the density of the texturing on the sample surface decreases. In Fig. 2a'-d′ the 3D morphology of the sample surface at different scanning spacings is shown. It is observed that the periodic weaving pattern is uniformly distributed on the sample, and the microstructure of the surface becomes quite porous and rough, which confirm the advantage of LST for surface morphology control [26]. After three Sa measurements by the 3D morphometer and averaging, Sa of 1.822 μm, 5.809 μm, 3.280 μm, and 2.105 μm are obtained for LM-0, LM-300, LM-600, and LM-900, respectively. It is further confirmed that rough porous nanostructure is formed on the surface of the samples. This can be attributed to the fact that the texturing density decreases with increasing spacing, while the percentage of smooth surfaces on the sample surface increases. Thus, choosing the appropriate LST spacing can modulate the surface morphology and roughness.

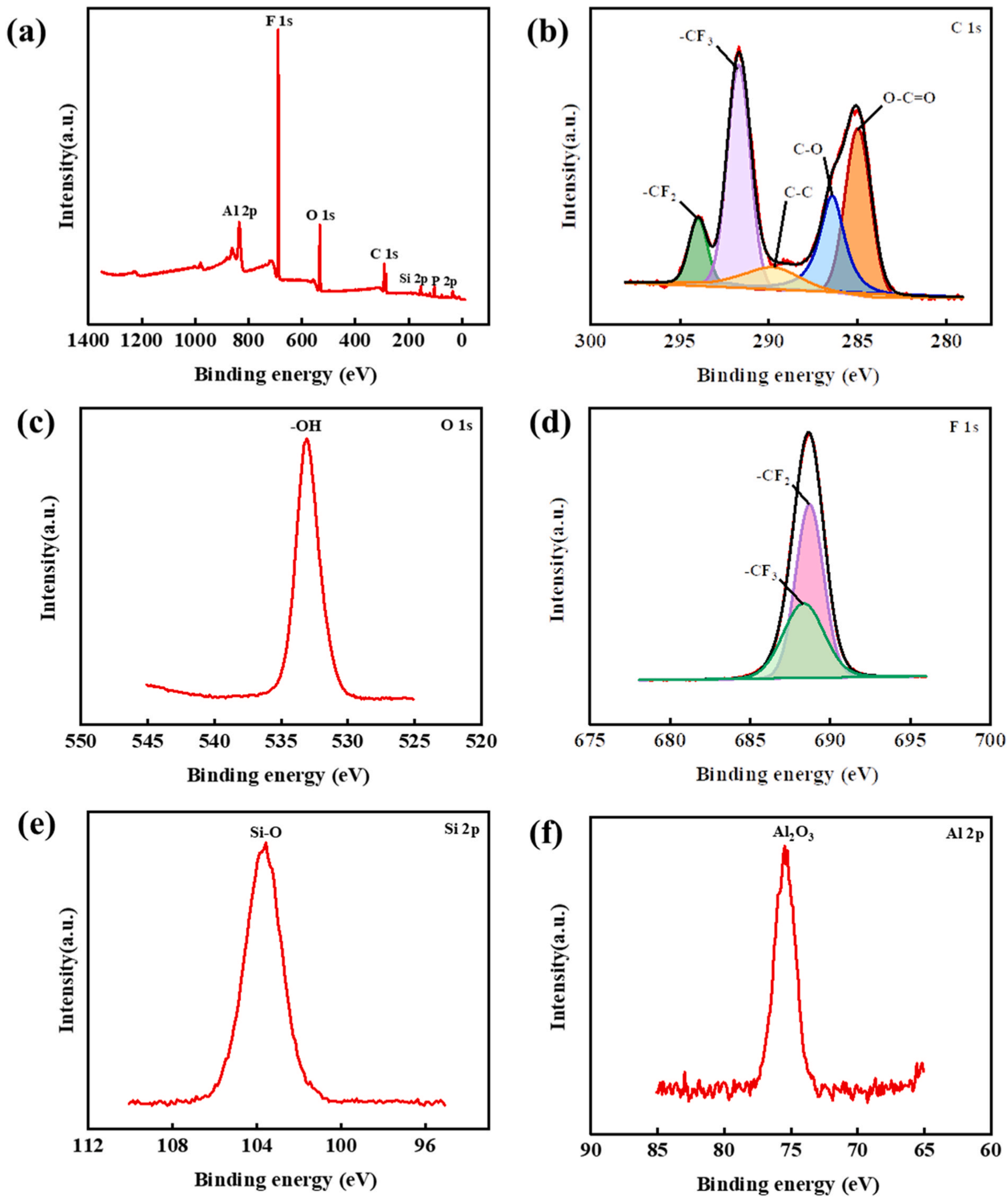

Fig. 4. (a) XPS spectrum of LM-300; (b)-(f) C 1 s, O 1 s, F 1 s, Al 2p, P 2p and Si 2p spectrums.

3.2. The analysis of SEM

In order to further characterize the surface morphology of the specimens, Fig. 3 further depicts the SEM morphology of the MAO Al disk and LM-300. As shown in Fig. 3a-b, the pits generated on the surface can be observed after the LST treatment. During laser processing, the material is subjected to high temperature heating, melting, sublimation and explosive ablation [27]. When the energy of the laser is sufficient to raise the temperature of the material to the vaporization threshold, the central portion of the laser irradiated material is instantaneously converted to a vapor state and removed. At the same time, the recoil pressure of the pulsed laser induces an outward jet of molten material from the melt pool. Under the combined effect of surface tension and gravity, the liquid molten material re-solidifies at the edge of the bath, forming an irregular re-melting layer [28,29]. In addition, material particles escaped from the surface and, subsequently, were deposited from the laser plume onto the surface around the irradiation zone in the form of micro- and nanoparticles [27,30]. Eventually, a hierarchical structure as shown in Fig. 3a is formed on the surface of the substrate after laser treatment. As shown in Fig. 3c-d, it can be clearly observed from them that the ceramic coating grows uniformly on the surface after LST treatment, a uniform rough and porous MAO coating is generated.

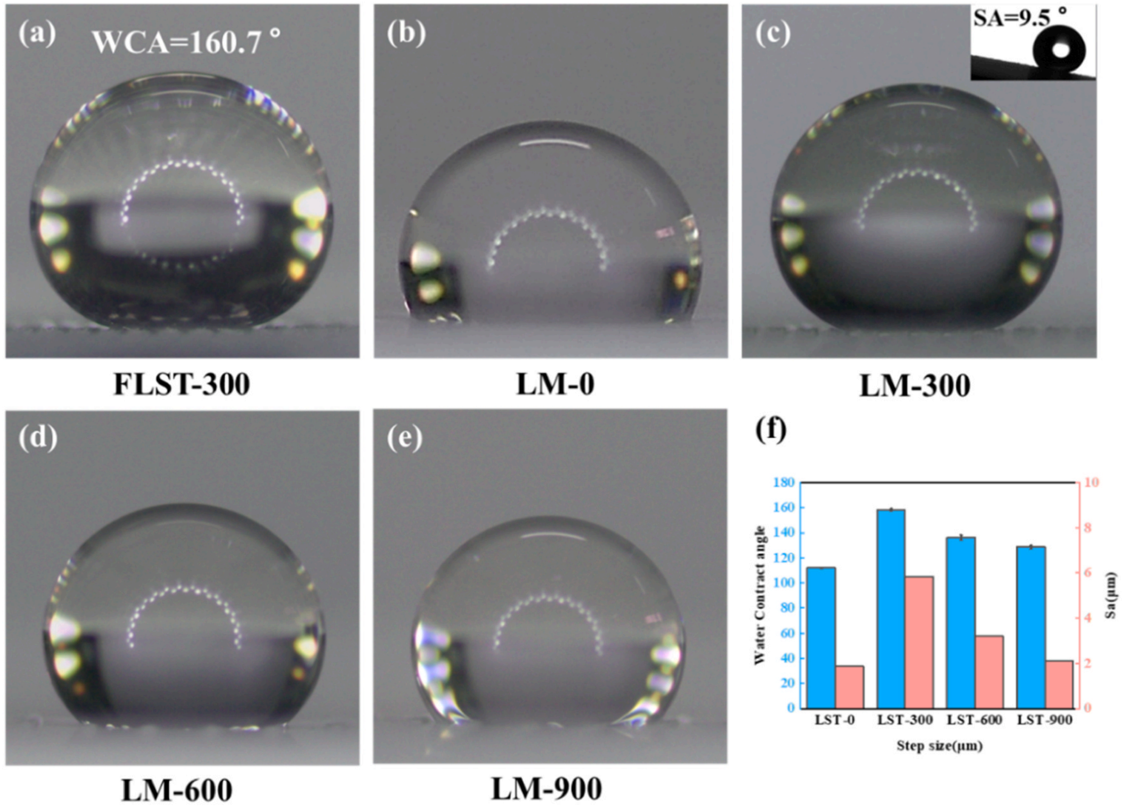

Fig. 5. WCA in air: (a)FLST-300; (b) LM-0; (c) LM-300; (d) LM-600; (e) LM-900; (f) WCA and Sa histogram for LM-0, LM-300, LM-600 and LM-900.

MAO coating is a metal oxide generated on the surface of the Al substrate under the effect of transient high temperature and high pressure generated by arc light discharge. Since many discharge channels are present, a ceramic coating with round "crater-like" holes is formed by the electrolyte [31,32]. The presence of MAO coating not only contributes to the abrasion and corrosion resistance of the Al disks, but also improves the mechanical stability of the superhydrophobic Al disks [33–35]. As the ceramic coating grows uniformly on the nanostructure formed after LST treatment, it covers the original structure. Therefore, after the LST and MAO treatments, a "double" nanostructure is formed on the surface, which is a combination of texturized pits formed by LST and ceramic coating formed by MAO. And this surface structure meets the requirements of micro-nanostructure needed for the construction of superhydrophobic surfaces [36,37], which can be used to construct superhydrophobic surfaces.

3.3. XPS analyses

To further investigate the elemental composition of the coatings and their forms of existence, the surface chemical composition of LM-300 is studied by XPS as shown in Fig. 4a-f. As shown in Fig. 4a, chemical elements including C, O, F, Al, P, and Si are clearly detected on the surface of LM-300. Among them, a large amount of Si and F is originated from the PFOCTS reagent. In Fig. 4b, the C 1 s spectra shows the presence of five peaks at 285.08 eV, 286.38 eV, 289.88 eV, 291.68 eV, and 293.98 eV, with values corresponding to the binding energies of O-C═O, C-O, C-C, $-CF_3$, and $-CF_2$, respectively. In Fig. 4c, the O 1 s spectra has a peak at 533.08 eV corresponding to the binding energy of -OH, indicating that the element O in the coating is mostly in the form of -OH, and a large number of hydroxyl groups exist on the sample surface. The F 1 s spectra in Fig. 4d have peaks at 688.68 eV and 688.38 eV corresponding to $-CF_2$ and $-CF_3$, respectively, further indicating the presence of $-CF_2$ and $-CF_3$ functional groups. In Fig. 4e the peak in the Si 2p spectra is 103.58 eV, which corresponds to the binding energy of the Si-O. The binding energy of the Al 2p peak is 75.8 eV [38], indicating the presence of Al_2O_3 in Fig. 2f. According to studies, $-CF_2$ and $-CF_3$ functional groups tend to cause surface fluorination and reduce surface energy, which results in superhydrophobicity [39]. The above experimental results show that Si-O, $-CF_3$ and $-CF_2$ functional groups exist on the surface of LM-300. This indicates that perfluorooctylsilane ($Si-C_8H_4F_{13}$) is successfully grafted onto the surface of the sample during the fluorination process [40], which is conducive to the reduction of the surface energy of LM-300.

3.4. Wettability analysis

The WCA in air is measured for four samples, as shown in Fig. 5a-e. In Fig. 5a, the WCA of FLST-300 is 160.7 °, while the WCA of LM-300 is 158.3 °. It can be seen that there is little difference between the WCA of the FLST-300 and the WCA of the MAO-treated LM-300, and both have a WCA greater than 150 °. In addition, the roll-off angle of LM-300 is 9.5 °, which indicates that a composite coating with superhydrophobicity is prepared after LST/MAO treatment and hydrophobization. Moreover, the composite coating surface has a "double" micro-nanostructure consisting of rough and porous "crater" micro-nanostructures and textured craters formed by LST, which will lead to the formation of air pockets between the liquid droplets and the micro-nanostructures, and the formation of a non-homogeneous wetting system consisting of composite interfaces combining solids, liquids, and gases. This can be explained by the Cassie-Baxter model [41]. In the Cassie-Baxter mechanism, air fills and occupies the hollow space of the rough microstructure, thus forming a composite interface consisting of air pockets and solids to support the water droplets. As the microstructure of the material surface holds a certain amount of air, it reduces the contact area between the water droplets and the material surface, decreases the adhesion between the water droplets and the surface, and makes the water droplets on the surface easy to slip off from the surface [42,43], which further enhances the hydrophobicity. The following equation is used for representation

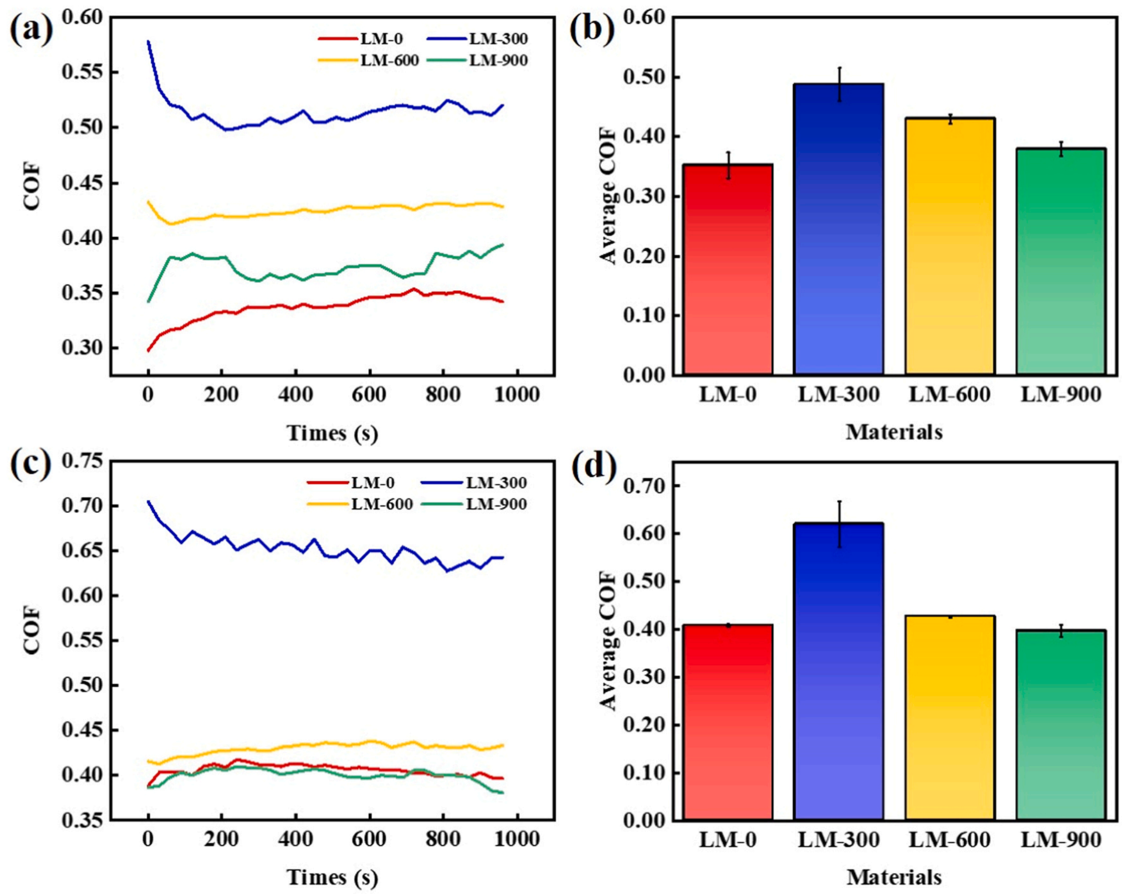

Fig. 6. COF of LM-0, LM-300, LM-600 and LM-900 under dry friction conditions: (a) Instantaneous COF, (b) Average COF; COF of LM-0, LM-300, LM-600 and LM-900 under water lubrication conditions: (c) Instantaneous COF, (d) Average COF.

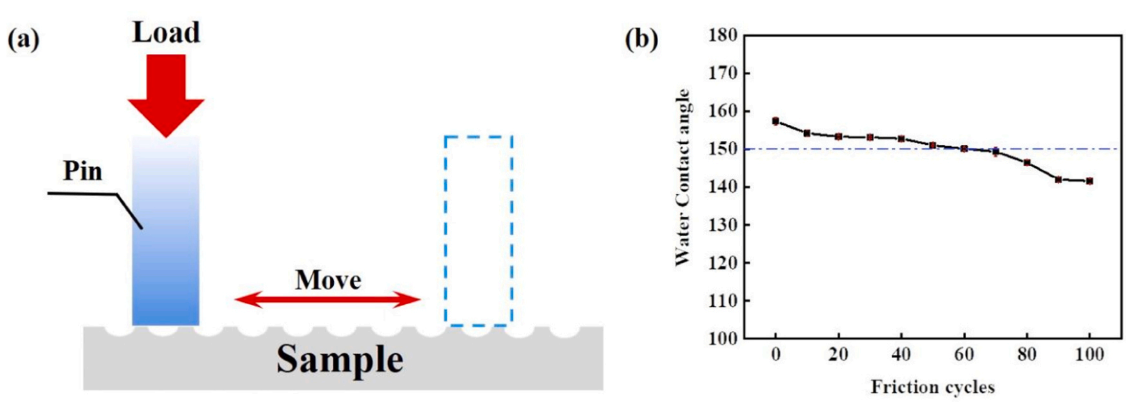

Fig. 7. (a) Schematic diagram of cyclic abrasion test; (b) WCA of LM-300 surface under different friction cycles.

[44] :

$$\cos\theta_C = f_s(r_{sl}\cos\theta + 1) - 1$$

In the formula, θ_c is the actual contact angle of the hydrophobic surface; r_{sl} is the dimensionless surface roughness factor, defined by the ratio of the actual area of the rough surface; and f_s is the fraction of the area of the liquid-gas interface that is obscured by the surface texture; and θ is the equilibrium contact angle on the solid. In Fig. 5f, the WCA of LM-0, LM-300, LM-600 and LM-900 are 112.1 °, 158.3 °, 136.2 ° and 128.5 °, respectively, and the WCA show a tendency of increasing and then decreasing. In addition, the Sa of the samples increases and then decreases as the texture spacing goes from 0 to 900 μm, and peaks at 300 μm, which corresponds to the trend of WCA change. This result also confirms that the variation in WCA is related to the texture spacing [45, 46]. Additionally, as the scanning spacing becomes larger, the untreated area on the surface increases significantly, increasing the adhesion of droplets to the surface [47], which leads to a decrease in hydrophobicity. From the Cassie-Baxter model, an increase in the liquid-gas interfacial fraction and a decrease in the solid-liquid interfacial fraction of a superhydrophobic surface can enhance its hydrophobicity [40]. And a higher Sa value means more air is trapped in the surface microstructure, which makes the surface present a higher WCA. Therefore, it can be hypothesized that the LM-300 specimen can trap more air in the surface structure, which increases the proportion of the liquid-air

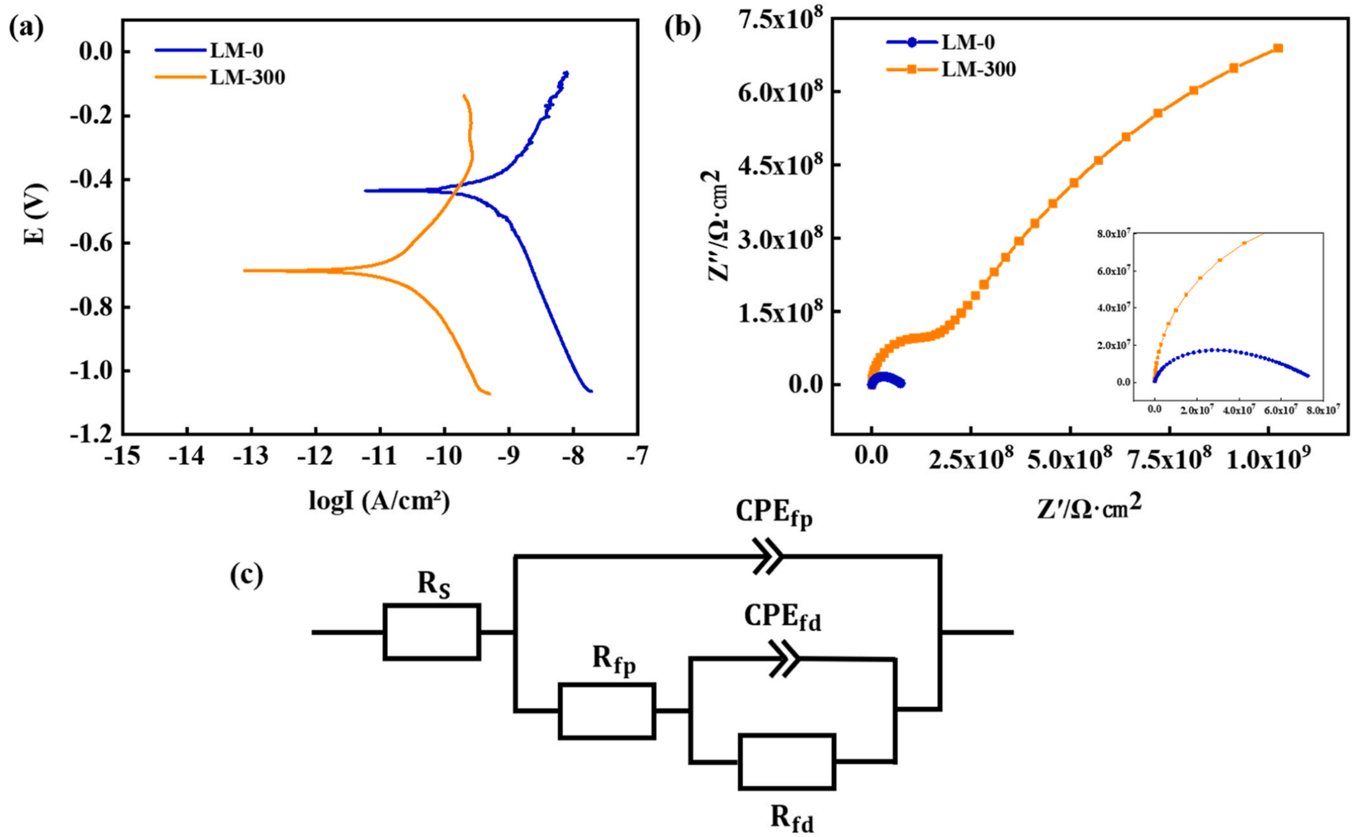

Fig. 8. Polarization curves and Nyquist curves of LM-0 and LM-300 specimens in 3.5 wt% NaCl solution.

Table 1
Parameters of Nyquist curves of LM-0 and LM-300 specimens in 3.5 wt% NaCl solution.

Sample	Corrosion potential E_{corr} (V)	Corrosion current I_{corr} (A/cm^2)	Corrosion rate mm/a
LM-0	-0.43449	2.4E-09	2.8E-05
LM-300	-0.68618	7.6E-11	8.9E-07

interface, which leads to a higher WCA.

3.5. Friction experiments

As shown in Fig. 6, the friction properties of the hydrophobic surfaces are evaluated with a ball-and-disc friction machine, as well as analyzing the effects of changes in laser texturing spacing and hydrophobicity on the friction properties of the samples. In Fig. 6a-b, the COF of LM-0, LM-300, LM-600 and LM-900 under dry friction conditions are presented as a function of time. In Fig. 6a, under dry friction conditions, the instantaneous COF of LM-300 and LM-600 samples start to decrease suddenly at 120 s, and then gradually stabilize in the later period. In Fig. 6b, the average COF of LM-0, LM-300, LM-600, and LM-900 are 0.351, 0.486, 0.429, and 0.398, respectively. And the highest average COF is found in LM-300 and the lowest in LM-0. Additionally, as shown in Fig. 6c, the transient COF of LM-300 decreases and then smooths out under water friction conditions, while the overall transient COF of LM-0, LM-600, and LM-900 are relatively stable. In Fig. 6d, the average COF of LM-0, LM-300, LM-600, and LM-900 are 0.408, 0.621, 0.427, and 0.397, respectively. And the average COF of LM-300 is the highest, and that of LM-0 is the lowest. These are nearly consistent with the trends in Fig. 6a and Fig. 6b, respectively. For the trend in the friction curves of the LM-300 and LM-600, which can be attributed to the continuous formation of abrasive debris on the wear surfaces, while the debris fills the pits of the texture. As well as the fact that the polyethylene balls are self-lubricating, adhesive abrasion occurs during the abrasion process due to adhesion. Therefore, the COF decreases and gradually steadies [48]. In contrast, the instantaneous COF of LM-0 and LM-900 increased and then leveled off at 120 s. The possible reasons for this are that the density of pits distributed on the surface decreases as the spacing of the texturing increases, the surface roughness decreases, and only a small portion of the friction-generated abrasive debris fills the pits, while the rest of the debris undergoes abrasive wear. As the abrasion debris continuously falls off, the COF increases and gradually stabilizes over time. In addition, there is no texture on the surface of LM-0 to collect abrasive debris, so adhesive wear occurs as the debris continues to fall, and a lubricant film can be generated more quickly on the abraded surface, resulting in a smaller COF. For hydrophobic-hydrophobic friction partners under water lubrication, the presence of water hardly plays a role in lubrication and friction reduction [49]. Moreover, under water lubrication, some of the debris is carried away by the water after each

Table 2
Parameters of Nyquist curves of LM-0 and LM-300 specimens in 3.5 wt% NaCl solution.

Sample	R_s(Ω·cm^2)	CPE_{fp}-T(F)	CPE_{fp}-P	R_{fp}(Ω·cm^2)	CPE_{fd}-T(F)	CPE_{fd}-P	R_{fd}(Ω·cm^2)
LM-0	2779.7	1.4E-10	0.95249	1.5E+06	3.1E-09	0.39676	7.6E+07
LM-300	-3104.5	9.0E-11	0.98819	1.6E+08	2.1E-09	0.62452	3.0E+09

friction and hardly participates in the friction process [21], so the accumulation of abrasive debris in the pits is reduced compared to dry friction, which in turn increases the actual contact area and leads to an increase in the COF. The above results indicate that the variation of the texture spacing can change the actual contact area between the friction balls and the surface, thus affecting the friction performance.

3.6. Abrasion experiment

The poor mechanical durability of superhydrophobic surfaces has been a limiting factor in their widespread use in practice, with even minor abrasion damaging the surface structure and affecting hydrophobicity [50]. The abrasion resistance of LM-300 is tested here by pin-disk abrasion experiment. Fig. 7a shows a schematic diagram of the pin-disc reciprocation test of a zirconia ceramic rod on the surface of LM-300. Fig. 7b shows the WCA of LM-300 under different abrasion cycles. It can be seen that as the number of abrasion times increases from 0 to 61 and the moving distance is 122 cm, the WCA decreases from 158.3 ° to 148.2 ° and the surface loses its superhydrophobicity. This is likely due to an increase in the number of abrasion cycles, leading to the degradation of surface nanostructure and a reduction in surface fluorine concentration, gradually resulting in the loss of superhydrophobicity. For example, in the study of Wei [51] et al. chemical etching and stearic acid modification were used to obtain superhydrophobic surfaces, but since stearic acid itself is a fatty acid, which belongs to the softer substances, its abrasion resistance is relatively poor. In our study, the prepared superhydrophobic surface is able to withstand cyclic abrasion of ceramic zirconia for 61 cycles at a pressure of approximately 2.5 kPa. Therefore, the prepared LM-300 surface has some improvement in mechanical stability compared to other similar superhydrophobic surfaces. This may be attributed to the fact that the ceramic coating on the surface improves its mechanical properties, which results in higher abrasion resistance.

3.7. Electrochemical corrosion experiment

In order to further investigate the anticorrosion efficiency of laser chemically treated superhydrophobic surfaces, electrochemical measurements are also performed on various types of surfaces prepared in this work. The experiment is carried out in 3.5 wt% NaCl solution. As shown in Fig. 8, the corrosion resistance of the samples (LM-0, LM-300) is studied using polarization curves and Nyquist curves. Fig. 8c in the equivalent circuit using the parameters R_s、R_{fp}、R_{fd}、CPE_{fp} and CPE_{fd} to fit the EIS data. R_s represents the solution resistance, R_{fp} represents the resistance of the loose outer and dense inner layers of the MAO coating, while CPE_{fp} and CPE_{fd} represent constant phase elements connected in parallel with R_{fp} and R_{fd}, respectively. The polarization curves of LM-0 and LM-300 are shown in Fig. 8a. There values of corrosion potential (E_{corr}), corrosion current (I_{corr}) and corrosion rate are listed in Table 1. As shown in the experimental results, the laser chemically treated superhydrophobic surface (LM-300) exhibits lower corrosion currents compared to the untreated surface (LM-0) From Table 1, it can be seen that the corrosion current decreased by two orders of magnitude from 2.4E-09–7.6E-11. According to the electrochemical corrosion characteristics, the smaller the corrosion current, the smaller the self-corrosion reaction rate [52]. Also as shown in the Nyquist plot in Fig. 8b, it can be seen that LM-300 exhibits a larger diameter semicircle, which represents a better corrosion resistance [53]. From the above results, on the one hand, we believe that it is due to the fact that the rough superhydrophobic surface can form a film of air between the corrosive liquid and the specimen, which protects the specimen and the corrosive liquid from direct contact. On the other hand, the hydrophobic layer acts as a barrier to inhibit chloride ion adsorption [54], while the MAO coating with good corrosion resistance acts as a physical barrier. Therefore, through the synergistic effect of these factors, the corrosion resistance of the composite coating is improved to a certain extent, giving LM-300 better anti-corrosion performance.

4. Conclusions

In this work, we have prepared a novel superhydrophobic surface using an approach based on LST and MAO techniques combined with chemical immersion treatment. The surface is superhydrophobic with a WCA of about 158.3 ° and the roll-off angle of about 9.5 °. It also has good mechanical durability. This is due to the combined effect of the "double" nanostructure formed by the MAO coating and the laser texturing and the chemical modification of the surface. In addition, the superhydrophobic coating showed excellent mechanical stability under 100 cycles at 2.5 kPa in abrasion experiment. Meanwhile, in electrochemical corrosion experiment, the corrosion current density of LM-300 was 2 orders of magnitude lower compared to LM-0, which exhibited better corrosion resistance. They were attributed to the fact that MAO improves the abrasion and corrosion resistance of the coatings, increasing the service life of the coatings in harsh environments. In friction experiment, the COF of LM-300 was the largest, which was due to the incomplete lubrication film formed on the friction surface, resulting in reduced lubrication effectiveness. As a result, this work successfully prepared a novel superhydrophobic coating with stable mechanical durability.

Author statement

The manuscript “Preparation Preparation of mechanically durable superhydrophobic aluminum surfaces by LST/MAO and chemical modification” was completed by Qiqi Wu, Jing Xu, Nan Tu, Bowen Xue, Jian Chen and Hailin Lu. This work is original research which has not been published previously, and not under consideration for publication elsewhere.

CRediT authorship contribution statement

Jing Xu: Writing – review & editing, Funding acquisition. **Wu Qiqi:** Writing – original draft. **Nan Tu:** Writing – review & editing, Conceptualization. **Bowen Xue:** Writing – review & editing, Methodology. **Jian Chen:** Writing – review & editing, Data curation. **Hailin Lu:** Writing – review & editing, Resources, Funding acquisition.

Declaration of Competing Interest

The authors declare that they have no known competing financial interests or personal relationships that could have appeared to influence the work reported in this paper.

Data availability

Data will be made available on request.

Acknowledgements

This work was supported by National Natural Science Foundation of China (No. 52005381).

References

[1] Y.B. Liu, K. Fu, J. Liu, Y. Tian, H. Zhang, R.M. Wang, B.L. Zhang, H.P. Zhang, F. T. Zhou, Q.Y. Zhang, Design and preparation of a multi-fluorination organic superhydrophobic coating with high mechanical robustness and icing delay ability, Appl. Surf. Sci. 497 (2019) 8.

[2] Z.A. Liu, X.L. Yang, G.B. Pang, F. Zhang, Y.Q. Han, X.Y. Wang, X. Liu, L. Xue, Temperature-based adhesion tuning and superwettability switching on superhydrophobic aluminum surface for droplet manipulations, Surf. Coat. Technol. 375 (2019) 527–533.

[3] Y.Q. Qing, C. Long, K. An, C.B. Hu, C.S. Liu, Sandpaper as template for a robust superhydrophobic surface with self-cleaning and anti-snow/icing performances, J. Colloid Interface Sci. 548 (2019) 224–232.
[4] Z.X. Lv, S.R. Yu, K.X. Song, X. Zhou, X.L. Yin, Fabrication of a leaf-like superhydrophobic CuO coating on 6061Al with good self-cleaning, mechanical and chemical stability, Ceram. Int. 46 (2020) 14872–14883.
[5] S.S. Xu, Q. Wang, N. Wang, X. Zheng, Fabrication of superhydrophobic green surfaces with good self-cleaning, chemical stability and anti-corrosion properties, J. Mater. Sci. 54 (2019) 13006–13016.
[6] W.H. Yao, L. Wu, G.S. Huang, B. Jiang, A. Atrens, F.S. Pan, Superhydrophobic coatings for corrosion protection of magnesium alloys, J. Mater. Sci. Technol. 52 (2020) 100–118.
[7] H.J. Yang, Y.M. Gao, G.S. Frankel, W.C. Qin, T.S. Li, Z.F. Huang, L. Wu, Robust superhydrophobic surface with reinforced skeletons for corrosion protection, Appl. Surf. Sci. 499 (2020) 15.
[8] L.B. Feng, Y.L. Zhu, J. Wang, X.T. Shi, One-step hydrothermal process to fabricate superhydrophobic surface on magnesium alloy with enhanced corrosion resistance and self-cleaning performance, Appl. Surf. Sci. 422 (2017) 566–573.
[9] Z.B. Zhang, F.X. Xue, W.X. Bai, X.T. Shi, Y.H. Liu, L.B. Feng, Superhydrophobic surface on Al alloy with robust durability and excellent self-healing performance, Surf. Coat. Technol. 410 (2021) 10.
[10] F. Zhang, H.C. Qian, L.T. Wang, Z. Wang, C.W. Du, X.G. Li, D.W. Zhang, Superhydrophobic carbon nanotubes/epoxy nanocomposite coating by facile one-step spraying, Surf. Coat. Technol. 341 (2018) 15–23.
[11] G.Q. Xin, C.Y. Wu, H.Y. Cao, W.N. Liu, B. Li, Y. Huang, Y.M. Rong, G.J. Zhang, Superhydrophobic TC4 alloy surface fabricated by laser micro-scanning to reduce adhesion and drag resistance, Surf. Coat. Technol. 391 (2020) 10.
[12] N.G. Tran, D.M. Chun, Simple and fast surface modification of nanosecond-pulse laser-textured stainless steel for robust superhydrophobic surfaces, CIRP Ann. -Manuf. Technol. 69 (2020) 525–528.
[13] B.J. Li, H. Li, L.J. Huang, N.F. Ren, X. Kong, Femtosecond pulsed laser textured titanium surfaces with stable superhydrophilicity and superhydrophobicity, Appl. Surf. Sci. 389 (2016) 585–593.
[14] R. Liu, Z.D. Chi, L. Cao, Z.K. Weng, L. Wang, L. Li, S. Saeed, Z.X. Lian, Z.B. Wang, Fabrication of biomimetic superhydrophobic and anti-icing Ti6Al4V alloy surfaces by direct laser interference lithography and hydrothermal treatment, Appl. Surf. Sci. 534 (2020) 8.
[15] H.P. Gao, Y. Liu, G.Y. Wang, S.Y. Li, Z.W. Han, L.Q. Ren, Biomimetic metal surfaces inspired by lotus and reed leaves for manipulation of microdroplets or fluids, Appl. Surf. Sci. 519 (2020) 11.
[16] D.V. Ta, A. Dunn, T.J. Wasley, R.W. Kay, J. Stringer, P.J. Smith, C. Connaughton, J. D. Shephard, Nanosecond laser textured superhydrophobic metallic surfaces and their chemical sensing applications, Appl. Surf. Sci. 357 (2015) 248–254.
[17] L.B. Boinovich, A.M. Emelyanenko, A.D. Modestov, A.G. Domantovsky, K. A. Emelyanenko, Synergistic Effect of Superhydrophobicity and Oxidized Layers on Corrosion Resistance of Aluminum Alloy Surface Textured by Nanosecond Laser Treatment, ACS Appl. Mater. Interfaces 7 (2015) 19500–19508.
[18] J.Y. Jiang, J.L. Xu, Z.H. Liu, L. Deng, B. Sun, S.D. Liu, L. Wang, H.Y. Liu, Preparation, corrosion resistance and hemocompatibility of the superhydrophobic TiO2 coatings on biomedical Ti-6Al-4V alloys, Appl. Surf. Sci. 347 (2015) 591–595.
[19] Z.X. Lian, J.K. Xu, Z.J. Yu, P. Yu, W.F. Ren, Z.B. Wang, H.D. Yu, Bioinspired Reversible Switch between Underwater Superoleophobicity/Superaerophobicity and Oleophilicity/Aerophilicity and Improved Antireflective Property on the Nanosecond Laser-Ablated Superhydrophobic Titanium Surfaces, ACS Appl. Mater. Interfaces 12 (2020) 6573–6580.
[20] A. Fihri, E. Bovero, A. Al-Shahrani, A. Al-Ghamdi, G. Alabedi, Recent progress in superhydrophobic coatings used for steel protection: a review, Colloid Surf. A Physicochem. Eng. Asp. 520 (2017) 378–390.
[21] C.K. Wang, H.L. Lu, H.Y. Yang, B.W. Xue, E.D. Jia, G.Q. Chai, The effect of adding polyethylene glycol to electrolyte solution on micro-arc oxidation coating on pure aluminum, Appl. Surf. Sci. 599 (2022) 11.
[22] J.F. Chen, W.X. Lin, S.Y. Liang, L.C. Zou, C. Wang, B.S. Wang, M.F. Yan, X.P. Cui, Effect of alloy cations on corrosion resistance of LDH/MAO coating on magnesium alloy, Appl. Surf. Sci. 463 (2019) 535–544.
[23] G.Q. Chai, H.L. Lu, B.W. Xue, E.D. Jia, H.Y. Yang, C.K. Wang, Effect of liquid crystal polymer micro-bump structure prepared by mesh method on the frictional corrosion performance of micro-arc oxide coated pure aluminum disks, Surf. Coat. Technol. 446 (2022) 13.
[24] B.W. Xue, H. Lin, G.Q. Chai, C.K. Wang, H.Y. Yang, H.L. Lu, Micro-arc oxidation enhances the wear resistance and corrosion resistance of oil-water separating mesh, J. Mater. Sci. 57 (2022) 18370–18384.
[25] X.J. Cui, X.Z. Lin, C.H. Liu, R.S. Yang, X.W. Zheng, M. Gong, Fabrication and corrosion resistance of a hydrophobic micro-arc oxidation coating on AZ31 Mg alloy, Corros. Sci. 90 (2015) 402–412.
[26] Q. Ma, W. Wang, G.N. Dong, Facile fabrication of biomimetic liquid-infused slippery surface on carbon steel and its self-cleaning, anti-corrosion, anti-frosting and tribological properties, Colloid Surf. A-Physicochem. Eng. Asp. 577 (2019) 17–26.
[27] E.A. Kuzina, F.S. Omran, A.M. Emelyanenko, L.B. Boinovich, On the Significance of Selecting Hydrophobization Conditions for Obtaining Stable Superhydrophobic Coatings, Colloid J. 85 (2023) 59–65.
[28] A. Grabowski, M. Sozanska, M. Adamiak, M. Kepinska, T. Florian, Laser surface texturing of Ti6Al4V alloy, stainless steel and aluminium silicon alloy, Appl. Surf. Sci. 461 (2018) 117–123.
[29] J.R. Zhang, Y.C. Guan, W.T. Lin, X.N. Gu, Enhanced mechanical properties and biocompatibility of Mg-Gd-Ca alloy by laser surface processing, Surf. Coat. Technol. 362 (2019) 176–184.
[30] L.B. Boinovich, E.B. Modin, A.R. Sayfutdinova, K.A. Emelyanenko, A.L. Vasiliev, A. M. Emelyanenko, Combination of functional nanoengineering and nanosecond laser texturing for design of superhydrophobic aluminum alloy with exceptional mechanical and chemical properties, ACS Nano 11 (2017) 10113–10123.
[31] G.Q. Li, Y.P. Wang, L.P. Qiao, R.F. Zhao, S.F. Zhang, R.F. Zhang, C.M. Chen, X.Y. Li, Y. Zhao, Preparation and formation mechanism of copper incorporated micro-arc oxidation coatings developed on Ti-6Al-4V alloys, Surf. Coat. Technol. 375 (2019) 74–85.
[32] R. Gabor, T. Prymus, L. Cvrcek, V. Nehasil, J. Hlinka, M. Buril, M. Tokarcikova, J. Seidlerova, Final surface modification for better wear resistance of ceramic coating on cast AlSi10Mg alloy, Ceram. Int. 48 (2022) 37433–37447.
[33] N. Dudareva, L. Zaynullina, S. Kiseleva, M. Abramova, The influence of alloy microstructure on corrosion resistance and other properties of coatings formed by microarc oxidation, Mater. Chem. Phys. 288 (2022) 5.
[34] W.X. Sun, Y.P. Liu, T.H. Li, S.W. Cui, S.G. Chen, Q.L. Yu, D.A. Wang, Anti-corrosion of amphoteric metal enhanced by MAO/corrosion inhibitor composite in acid, alkaline and salt solutions, J. Colloid Interface Sci. 554 (2019) 488–499.
[35] W. Wang, C. Xin, Z.Q. Feng, G. Li, R.Z. Zhang, J.H. Hu, M.Q. Tang, Y.H. Liu, W. Zhang, Ceramic coatings by microarc oxidation of Ti and Al alloys, Surf. Interfaces 33 (2022) 8.
[36] C.L. Zhang, F. Zhang, L. Song, R.C. Zeng, S.Q. Li, E.H. Han, Corrosion resistance of a superhydrophobic surface on micro-arc oxidation coated Mg-Li-Ca alloy, J. Alloy. Compd. 728 (2017) 815–826.
[37] Z.Q. Zhang, L. Wang, M.Q. Zeng, R.C. Zeng, C.G. Lin, Z.L. Wang, D.C. Chen, Q. Zhang, Corrosion resistance and superhydrophobicity of one-step polypropylene coating on anodized AZ31 Mg alloy, J. Magnes. Alloy. 9 (2021) 1443–1457.
[38] E.D. Jia, H.L. Lu, G.S. Xu, B.W. Xue, C.K. Wang, G.Q. Chai, H.Y. Yang, J.H. Li, Polyvinyl alcohol/polyethylene glycol composite hydrogel parceling on aluminum: toward more robust micro-arc oxidation coatings, Ceram. Int. 49 (2023) 13081–13091.
[39] Q.H. Wang, A. Samanta, S.K. Shaw, H. Hu, H.T. Ding, Nanosecond laser-based high-throughput surface nanostructuring (nHSN), Appl. Surf. Sci. 507 (2020) 13.
[40] H.X. Wang, J. Zhuang, H.Y. Qi, J.T. Yu, Z.J. Guo, Y.H. Ma, Laser-chemical treated superhydrophobic surface as a barrier to marine atmospheric corrosion, Surf. Coat. Technol. 401 (2020) 12.
[41] A. Samanta, Q.H. Wang, S.K. Shaw, H.T. Ding, Roles of chemistry modification for laser textured metal alloys to achieve extreme surface wetting behaviors, Mater. Des. 192 (2020) 25.
[42] P.S. Brown, B. Bhushan, Mechanically durable, superomniphobic coatings prepared by layer-by-layer technique for self-cleaning and anti-smudge, J. Colloid Interface Sci. 456 (2015) 210–218.
[43] Y.G. Guo, X. Zhang, X.C. Wang, Q. Xu, T. Geng, Wetting and tribological properties of superhydrophobic aluminum surfaces with different water adhesion, J. Mater. Sci. 55 (2020) 11658–11668.
[44] A.M.A. Mohamed, A.M. Abdullah, N.A. Younan, Corrosion behavior of superhydrophobic surfaces: a review, Arab. J. Chem. 8 (2015) 749–765.
[45] S.A. Seyedmehdi, H. Zhang, J. Zhu, Superhydrophobic RTV silicone rubber insulator coatings, Appl. Surf. Sci. 258 (2012) 2972–2976.
[46] Y.Y. Yan, N. Gao, W. Barthlott, Mimicking natural superhydrophobic surfaces and grasping the wetting process: a review on recent progress in preparing superhydrophobic surfaces, Adv. Colloid Interface Sci. 169 (2011) 80–105.
[47] Z.X. Lian, J.K. Xu, P. Yu, Z.J. Yu, Z.B. Wang, H.D. Yu, Oil-repellent and corrosion resistance properties of superhydrophobic and superoleophobic aluminum alloy surfaces based on nanosecond laser-textured treatment, Met. Mater. Int. 26 (2020) 1603–1610.
[48] H.Y. Yang, X.F. Wu, S. Du, C.K. Wang, F. Guo, H.L. Lu, Synergistic effect of "double pores" texture on tribological properties of AZ31 Mg alloy micro-arc oxide ceramic coatings, Surf. Coat. Technol. 470 (2023) 11.
[49] Y.T. Cheng, D.E. Rodak, Is the lotus leaf superhydrophobic? Appl. Phys. Lett. 86 (2005) 3.
[50] R.Y. Sun, J. Zhao, Z. Li, J.L. Mo, Y.J. Pan, D.B. Luo, Preparation of mechanically durable superhydrophobic aluminum surface by sandblasting and chemical modification, Prog. Org. Coat. 133 (2019) 77–84.
[51] W. Tong, D.S. Xiong, N. Wang, C.Q. Yan, T. Tian, Green and timesaving fabrication of a superhydrophobic surface and its application to anti-icing, self-cleaning and oil-water separation, Surf. Coat. Technol. 352 (2018) 609–618.
[52] S.Q. Wang, Y.M. Wang, G. Cao, J.C. Chen, Y.C. Zou, B. Yang, J.H. Ouyang, D.C. Jia, Y. Zhou, Highly reliable double-layer coatings on magnesium alloy surfaces for robust superhydrophobicity, chemical durability and electrical property, Ceram. Int. 47 (2021) 35037–35047.
[53] J.H. Jiang, Q. Zhou, J.S. Yu, A.B. Ma, D. Song, F.M. Lu, L.Y. Zhang, D.H. Yang, J. Q. Chen, Comparative analysis for corrosion resistance of micro-arc oxidation coatings on coarse-grained and ultra-fine grained AZ91D Mg alloy, Surf. Coat. Technol. 216 (2013) 259–266.
[54] K.A. Emelyanenko, A.M. Emelyanenko, L.B. Boinovich, Laser obtained superhydrophobic state for stainless steel corrosion protection, a review, Coatings 13 (2023) 19.